University of Groningen

Observations of the planetary nebula SMP LMC 058 with the JWST MIRI medium resolution spectrometer

Jones, O. C.; Álvarez-Márquez, J.; Sloan, G. C.; Kavanagh, P. J.; Argyriou, I.; Law, D. R.; Labiano, A.; Patapis, P.; Mueller, Michael; Larson, Kirsten L.

IMPORTANT NOTE: You are advised to consult the publisher's version (publisher's PDF) if you wish to cite from it. Please check the document version below.

Document Version
Publisher's PDF, also known as Version of record

[Link to publication in University of Groningen/UMCG research database](#)

Observations of the planetary nebula SMP LMC 058 with the JWST MIRI medium resolution spectrometer

O. C. Jones [1]★ J. Álvarez-Márquez [2] G. C. Sloan [3,4] P. J. Kavanagh [5] I. Argyriou,[6] D. R. Law [3]
A. Labiano [7] P. Patapis [8] Michael Mueller [9] Kirsten L. Larson [3] Stacey N. Bright [3]
P. D. Klaassen [1] O. D. Fox [3] Danny Gasman [6] V. C. Geers,[1] Adrian M. Glauser [7]
Pierre Guillard [10,11] Omnarayani Nayak [3] A. Noriega-Crespo [3] Michael E. Ressler [12]
B. Sargent [3,13] T. Temim [14] B. Vandenbussche [6] and Macarena   García Marín [3]

[1]*UK Astronomy Technology Centre, Royal Observatory, Blackford Hill, Edinburgh, EH9 3HJ, UK*
[2]*Centro de Astrobiología (CSIC-INTA), Carretera de Ajalvir, 28850 Torrejón de Ardoz, Madrid, Spain*
[3]*Space Telescope Science Institute, 3700 San Martin Drive, Baltimore, MD 21218, USA*
[4]*Department of Physics and Astronomy, University of North Carolina at Chapel Hill, Campus Box 3255, Chapel Hill, NC 27599, USA*
[5]*Dublin Institute for Advanced Studies, School of Cosmic Physics, Astronomy & Astrophysics Section, 31 Fitzwilliam Place, Dublin 2, Ireland*
[6]*Institute of Astronomy, KU Leuven, Celestijnenlaan 200D, 3001 Leuven, Belgium*
[7]*Telespazio UK for the European Space Agency, ESAC, Camino Bajo del Castillo s/n, E-28692 Villanueva de la Cañada, Spain*
[8]*ETH Zurich, Institute for Particle Physics and Astrophysics, Wolfgang-Paulistr. 27, CH-8093 Zurich, Switzerland*
[9]*Kapteyn Astronomical Institute, Rijksuniversiteit Groningen, Postbus 800, 9700AV Groningen, the Netherlands*
[10]*Sorbonne Université, CNRS, UMR 7095, Institut d'Astrophysique de Paris, 98bis bd Arago, 75014 Paris, France*
[11]*Institut Universitaire de France, Ministére de l'Enseignement Supérieur et de la Recherche, 1 rue Descartes, 75231 Paris Cedex 05, France*
[12]*Jet Propulsion Laboratory, California Institute of Technology, 4800 Oak Grove Drive, Pasadena, CA 91109, USA*
[13]*Center for Astrophysical Sciences, The William H. Miller III Department of Physics and Astronomy, Johns Hopkins University, 3400 N. Charles Street, Baltimore, MD 21218, USA*
[14]*Princeton University, 4 Ivy Ln, Princeton, NJ 08544, USA*

ABSTRACT

During the commissioning of *JWST*, the medium-resolution spectrometer (MRS) on the mid-infrared instrument (MIRI) observed the planetary nebula SMP LMC 058 in the Large Magellanic Cloud. The MRS was designed to provide medium resolution ($R = \lambda/\Delta\lambda$) 3D spectroscopy in the whole MIRI range. SMP LMC 058 is the only source observed in *JWST* commissioning that is both spatially and spectrally unresolved by the MRS and is a good test of *JWST*'s capabilities. The new MRS spectra reveal a wealth of emission lines not previously detected in this planetary nebula. From these lines, the spectral resolving power ($\lambda/\Delta\lambda$) of the MRS is confirmed to be in the range $R = 4000$–1500, depending on the MRS spectral sub-band. In addition, the spectra confirm that the carbon-rich dust emission is from complex hydrocarbons and SiC grains and that there is little to no time evolution of the SiC dust and emission line strengths over a 17-yr epoch. These commissioning data reveal the great potential of the MIRI MRS for the study of circumstellar and interstellar material.

Key words: instrumentation: spectrographs – infrared: general – planetary nebulae: individual: SMP LMC 058.

1 INTRODUCTION

The succession of increasingly powerful mid-infrared spectrographs [e.g. the short wavelength spectrometer (SWS) and the infrared spectrograph (IRS) on board the *Infrared Space Observatory* and the *Spitzer Space Telescope*] launched into space has revolutionized our knowledge of the cool universe (e.g. Waters et al. 1996). For instance the resolving power of the ISO/SWS instrument ($R \sim 1300$–2500; de Graauw et al. 1996) provided a wealth of detections of line and continuum features never seen before. Whilst the sensitivity of the *Spitzer*/IRS (Houck et al. 2004) enabled mid-IR spectral observations

of a large number of individual objects in external galaxies (e.g. Zijlstra et al. 2006; Kemper et al. 2010).

The mid-infrared instrument (MIRI; Wright et al., submitted) on the JWST includes, in addition to the imager and coronographs, both a low-resolution spectrometer (LRS) covering wavelengths from 5 to 14 μm (Kendrew et al. 2015) and a medium-resolution spectrometer (MRS; Wells et al. 2015; Argyriou et al. 2023), which is an integral field unit (IFU), that has a field of view ranging from $3.2'' \times 3.7''$ to $6.6'' \times 7.7''$ (Law et al., submitted) and can spatially resolve spectroscopic data between 4.9 and 27.9 μm. This is the first time a mid-IR IFU has been deployed outside our atmosphere and through combining and improving upon the best attributes of both the SWS and IRS (namely their spectral resolution and sensitivity) will enable
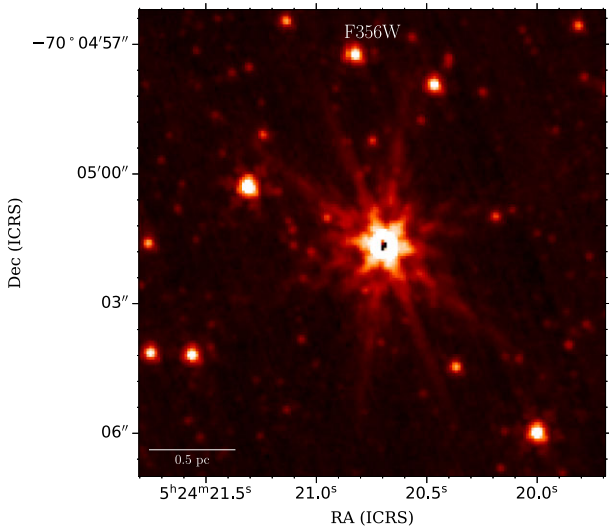
Figure 1. NIRCam F356W image of SMP LMC 058 shown in an Asinh stretch. At this spatial resolution (0.063″) SMP LMC 058 is an unresolved point source.

resolved spectroscopic studies of individual stars at the beginning and end of their evolution, diffuse structure in galaxies and planets.

The Large Magellanic Cloud (LMC) is a gas-rich, star-forming, irregular galaxy, which is a satellite of the Milky Way, hosts $\sim 10^3$ planetary nebulae (PNe) (Reid & Parker 2010; Reid 2014), and is at a uniform distance of ~ 50 kpc (Pietrzyński et al. 2013). In lower metallicity environments like the LMC, which has about half the metallicity of the Milky Way (Westerlund 1997; Choudhury, Subramaniam & Cole 2016), significant dust production is expected to occur in the outflows of asymptotic giant branch (AGB) stars with further processing as these objects become planetary nebula (PN). The gas and dust ejected into the interstellar medium (ISM) by a strong stellar wind from this phase of evolution contains elements synthesized in the stellar interior and dredged up to the surface by convection (e.g. Karakas & Lattanzio 2007, 2014). Their chemical composition is expected to primarily depend upon the initial stellar mass and the interstellar elemental abundance at the time the progenitor stars were formed (Kwok 2000; Gonçalves et al. 2014; Kwitter & Henry 2022).

As such, the infrared spectra of PNe host a rich variety of features; forbidden emission lines arising from ionization from the hot central star (e.g. Stanghellini et al. 2007), complex organic molecules (e.g. Ziurys 2006), polycyclic aromatic hydrocarbons (PAHs), and inorganic and organic solids (e.g. Stanghellini et al. 2007; Bernard-Salas et al. 2009; Guzman-Ramirez et al. 2011; García-Hernández & Górny 2014) with the frequency of carbonaceous features higher in the LMC than in Galactic PNe. This is likely due to the increased efficiency of third dredge-up (TDU) and the increased C/O ratio at low metallicities (Karakas, Lattanzio & Pols 2002). Processing by an external ambient UV radiation field which is stronger in the LMC (Gordon et al. 2008) may also affect the circumstellar chemistry. For instance, in this metallicity regime where elemental abundances are lower than those in the solar neighbourhood (but maybe comparable to the Galactic anticentre; Pagomenos, Bernard-Salas & Pottasch 2018) dust features like silicon carbide (SiC) become commonly observed. Detailed examination of PNe at sub-solar metallicity, therefore, provides a unique insight into chemical abundances and their effect on late-stage stellar evolution, dust production, and the

formation of PNe in conditions comparable to those during the epoch of peak star formation in the Universe (Madau et al. 1996). Furthermore, due to their compact nature and brightness over a broad wavelength range, PNe are also useful calibration sources (e.g. Swinyard et al. 1996; Feuchtgruber et al. 1997; Perley & Butler 2013; Brown, Jarrett & Cluver 2014).

SMP LMC 058 was observed by *JWST* as part of commissioning and calibration activities for MIRI. First identified by Sanduleak, MacConnell & Philip (1978), SMP LMC 058 is a carbon-rich PN in the LMC, with a heliocentric radial velocity of 278 ± 7 km s^{-1} (Margon et al. 2020). The central star of SMP 058 is a likely C II emitter (Margon et al. 2020) with a [WC] spectral type. Several dozen very strong, common emission lines of PNe were also detected in its optical spectra (Margon et al. 2020). SMP LMC 058 has also been observed with the *Spitzer* IRS at both low-resolution ($R \sim 60$–127) and high-resolution ($R \sim 600$). The Spitzer spectra show SMP LMC 058 has unusual dust chemistry with a strong SiC feature at ~ 11.3 μm (Bernard-Salas et al. 2009) and other associated features, including emission from PAHs at 6–9 μm, and a shoulder at 18 μm from an unidentified carrier. However, the Spitzer-IRS data show no clear evidence of fullerenes (Sloan et al. 2014). SiC is rarely seen in Galactic PNe, in spite of the higher Si abundance in the Milky Way compared to the Magellanic Clouds (Jones et al. 2017). Its strength may be due to photoexcitation, or because at a high C/O ratio SiC forms on the surface of carbon grains (Sloan et al. 2014).

In this paper, we describe the observations and calibration of *JWST* MIRI MRS commissioning data of SMP LMC 058 (Section 2). We then present its MRS spectra in Section 3 and determine the resolving power of the MRS in Section 4. In Section 5, we identify and analyse the new emission lines and solid-state features detected in this carbon-rich PN and compare this with *Spitzer* IRS data. The potential of the MRS and our conclusions are discussed in Section 6.

2 OBSERVATIONS AND CALIBRATIONS

The observations were taken as part of the MIRI MRS commissioning program, program ID 1049 [the commissioning purpose of these observations was point spread function (PSF) characterization]. They use the standard MRS observing template, with 4-point dither patterns optimized for channels 2, 3, and 4 respectively. Each dither pattern was used twice, in the 'positive' and 'negative' direction. Target acquisition was activated, with the science target itself serving as an acquisition target. All three bands (SHORT, MEDIUM, and LONG) in all channels were observed in all dithers. Simultaneous MIRI imaging in filter F770W was taken in the dither optimized for channel 2.

A dedicated background observation was taken, employing a 2-point dither optimized for all channels, on a field roughly 3 arcmin away. The background field was chosen to be relatively clear of astronomical sources based on archival WISE imaging data (Wright et al. 2010).

A total of 45 FASTR1 frames were taken per integration. In target observations, a single integration was taken per dither point. The background observation had two integrations (to match the total integration time on source, accounting for the use of only a two-point dither on the background). The integration time per MRS sub-band and complete dither were therefore 499.5 s or roughly 1500 s to cover the entire wavelength range (bands SHORT, MEDIUM, and LONG). Between the six dithers on-target and the single background, the total integration time was approximately 2.9 h (6.9 h including all overheads).
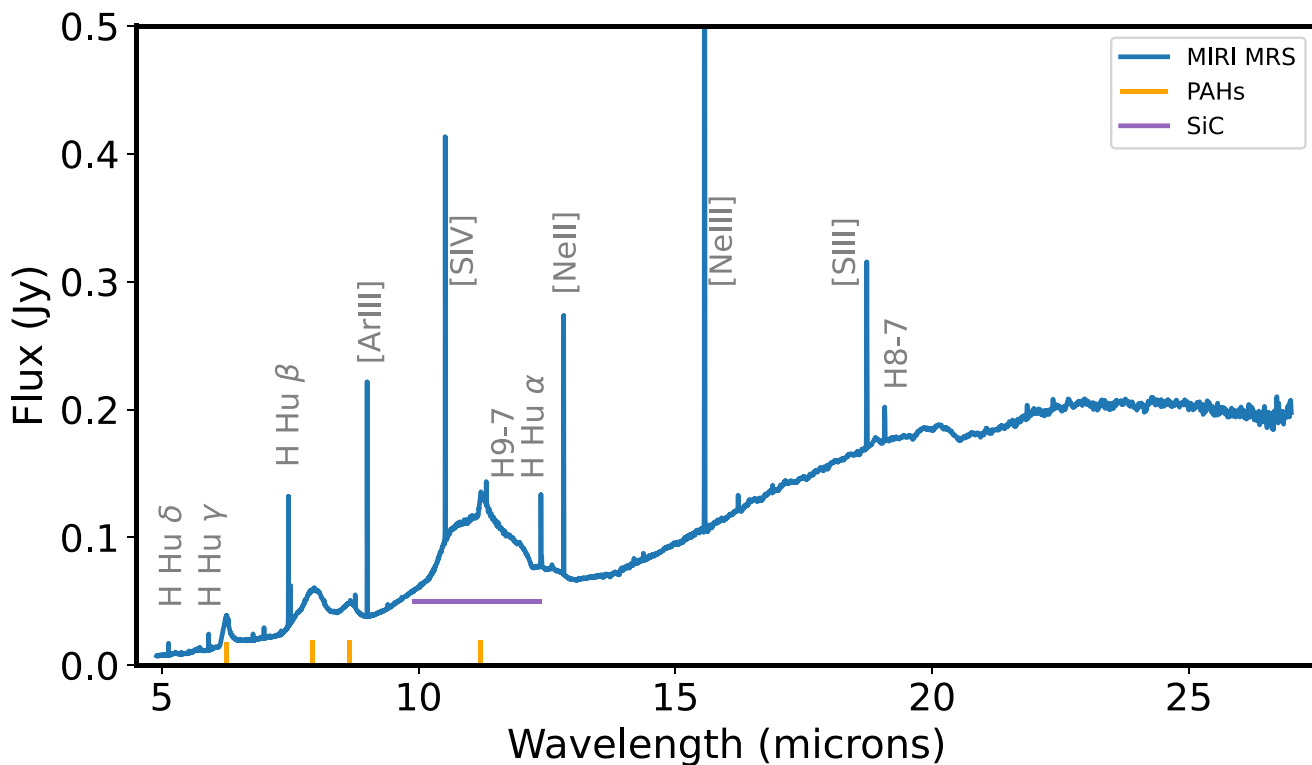
Figure 2. The MIRI MRS spectrum of SMP LMC 058. Numerous emission lines, PAH features, and dust features are clearly seen on a rising continuum. These features are much better resolved in the MRS spectra due to the higher spectral resolution. Artefacts at 12.2 μm and at $\sim$21 μm due to a dichroic spectral leak and as a result of stitching channels 4A and 4B are also present.

The MRS observations were processed with version 1.9.5 dev of the *JWST* calibration pipeline and context 1082 of the Calibration Reference Data System (CRDS). In general, we follow the standard MRS pipeline procedure (Labiano et al. 2016; Bushouse et al. 2022; and see Álvarez-Márquez et al. 2022 for an in-flight example of MRS data calibration). The background subtraction has been performed using the dedicated background observation. We have generated 12 3D spectral cubes, one for each of the MRS channels and bands, with a spatial and spectral sampling of 0.13" $\times$ 0.13" $\times$ 0.001 μm, 0.17" $\times$ 0.17" $\times$ 0.002 μm, 0.20" $\times$ 0.20" $\times$ 0.003 μm, and 0.35" $\times$ 0.35" $\times$ 0.006 μm for channels 1, 2, 3, and 4, respectively. The wavelength solution of the data cubes is designed to provide at least two samples per spectral resolution element (Law et al., submitted), consequently this Nyquist samples both the spatial PSF and the spectral line spread function (LSF) for each MRS channels. We have performed 1D spectral extractions individually in each of the MRS cubes using a circular aperture of radius equal to 1.5 $\times$ FWHM(λ), where FWHM(λ) = 0.3 arcsec for λ < 8 μm and FWHM(λ) = 0.31 $\times$ λ[μm]/8 arcsec for λ > 8 μm. The selected FWHM (λ) values follow the MRS PSF Full Width at Half Maximum (FWHM). NIRCam observation (see Fig. 1), and MRS observations suggest that SMP LMC 058 is an unresolved source. We use the MRS PSF models (Patapis et al., in preparation) to correct the aperture losses in the 1D spectra. The percentage of flux that is lost out of the selected aperture is 17 per cent for channel 1 and increases to 30 per cent in channel 4.

The 12 spectral segments extracted from these cubes were corrected for residual fringing using a post-pipeline spectral-level correction, which is a modified version of the detector-level correction available in the JWST calibration pipeline. The residual fringe contrasts are reduced by employing an empirical multicomponent sine fitting method (e.g. Kester, Beintema & Lutz 2003), under the assumption that the pipeline fringe flat correction has reduced fringe contrasts to the point where this multicomponent sine approximation is valid (Kavanagh et al., in preparation).

Finally, each of the 12 individual spectral segments was stitched together to remove minor flux discontinuities. This was done by determining a scaling factor between the median flux (excluding spectral lines) in the overlapping MRS segments; then applying this multiplicative factor to the longer wavelength segments, in turn, to effectively shift the spectrum to match the flux of its neighbouring shorter wavelength segment. This factor was typically on the order of 2 per cent–5 per cent, except for channel 4B which required a 9-per cent scaling. The flux data in the overlapping spectral regions were then averaged. The final stitched spectrum was inspected to ensure there were no remaining discontinuities, which may affect the continuum and model fitting.

3 SMP LMC 058 SPECTRUM

Fig. 2 shows the extracted spectrum of SMP LMC 058, which exhibits a rich variety of atomic, molecular, and solid state features, including PAHs and SiC, characteristic of carbon-rich material, and a strong continuum, which rises towards the longest wavelengths. Due to the superior sensitivity and spectral resolution (see Section 4) of the MRS, the MIRI spectrum of SMP LMC 058 shows features that are not seen in the *Spitzer* IRS data (see Section 5), notably in the number of emission lines detected.

In the spectrum presented here, there is a large amount of fine-structure line emission present, from the strong nebular forbidden lines of [Ar II], [Ar III], [S IV], [Ne II], [Ne III], and [S III] to weak H recombination lines (H I) from the Pfund and Humphreys
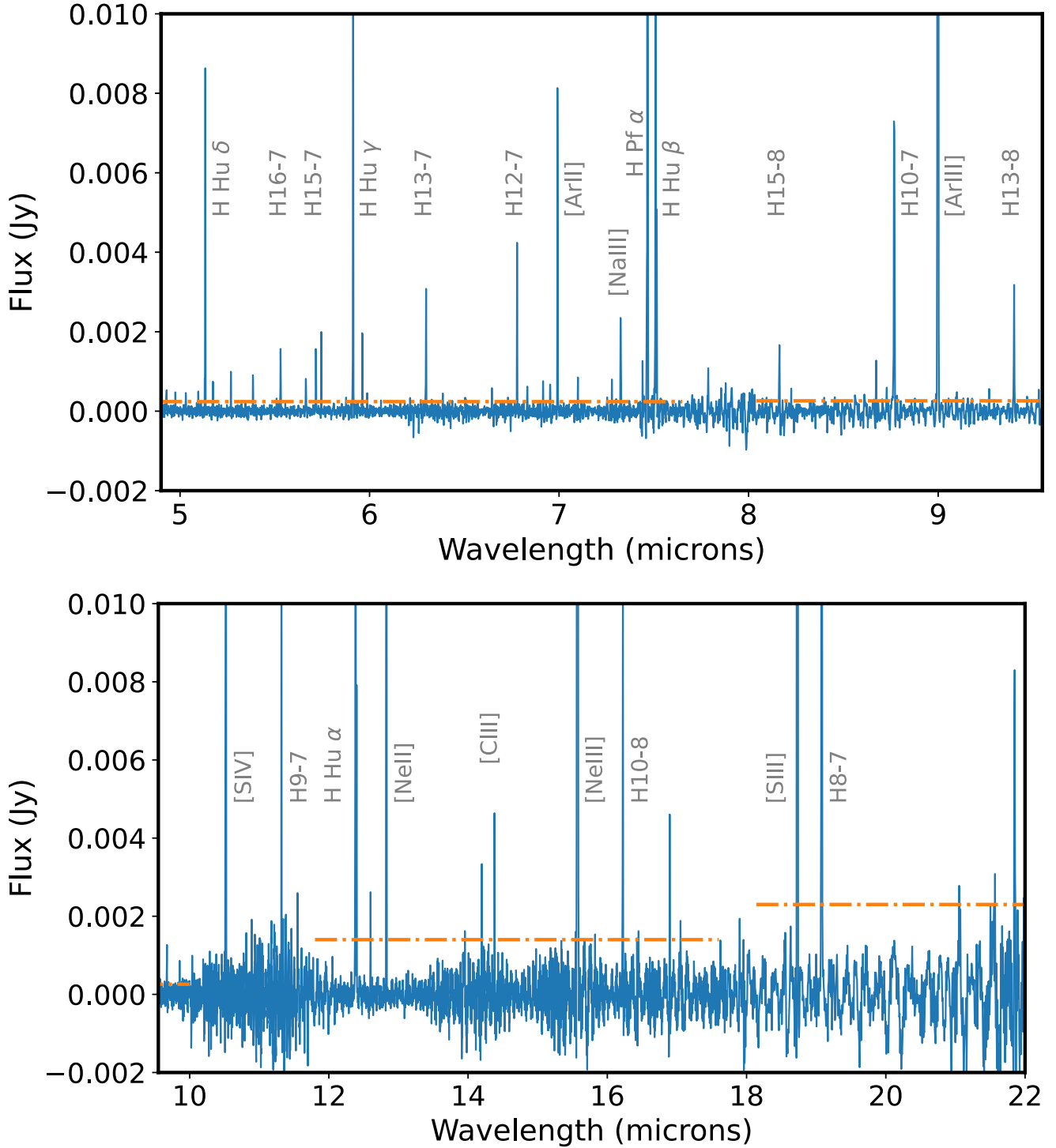
Figure 3. Continuum-subtracted MRS spectrum of SMP LMC 058 (where the continuum includes dust and PAH features), highlighting the atomic emission lines. The identification of key species are marked on the spectrum. The top panel shows lines in channels 1 and 2 of the MRS, and the lower panels show channels 3 and 4. The orange horizontal dashed lines denote the 3σ level above the continuum for each MRS channel, a gap is present where there is a band join between channels or complex continuum emission resulting in an increase in the S/N. The flux axis is truncated to highlight lower contrast lines.

series, and beyond. To ensure we measure and identify all the emission lines in the spectra we fit a pseudo-continuum to the broadband spectral features using a piece-wise spline model. Obvious narrow band features were identified and masked in the fitting

based on their amplitudes exceeding a threshold value. We used an outlier rejection fitter to flag and ignore any weaker narrow-band features that may compromise the continuum fit. After visual inspection of the fit, it was subtracted to isolate any narrow-band
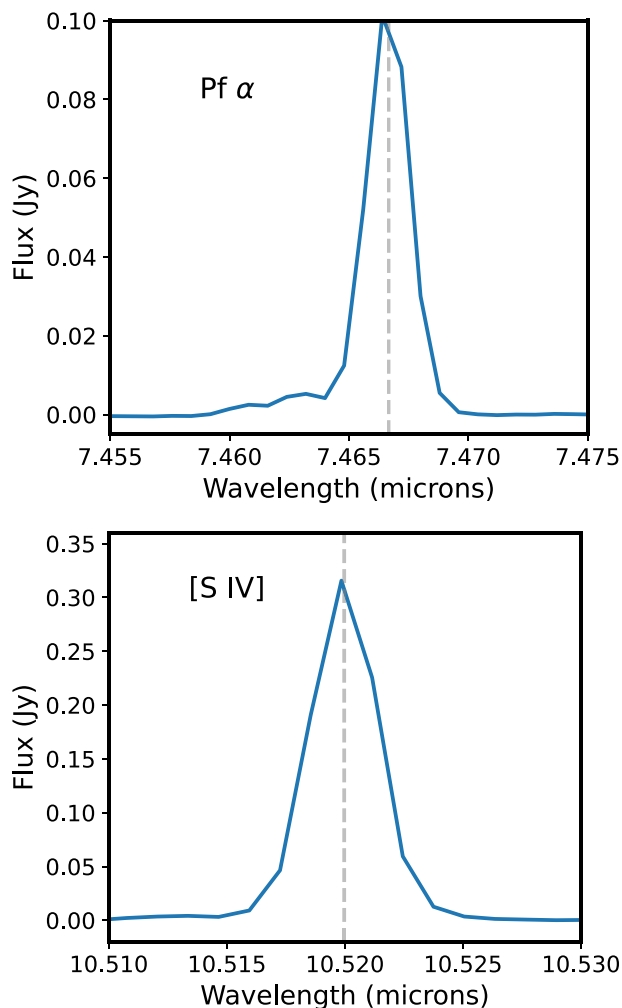
Figure 4. Top: the Pf α H I emission line profile shows a spatially unresolved main component and a weaker spectrally resolved blue-shifted wing. Bottom: the [S IV] line profile is spectrally unresolved and symmetric. This shape is typical of all the forbidden emission lines in SMP LMC 058. The dashed line marks the lines observed central wavelength.

features present. Fig. 3 shows the spectrum of SMP LMC 058 after subtraction of the pseudo-continuum from the total spectrum. The spectrum is extremely rich in emission lines. In total 51 lines were detected.

Using the 12 original MRS segments, we identified and analysed all detected emission lines with a signal-to-noise ratio (SNR) greater than 3 in the SMP LMC 058 spectra. These individual segments were scaled to remove flux discontinuities prior to measuring the line strengths. Depending on the line profiles (see Fig. 4), we performed one-component and two-component Gaussian fits, plus a second-order polynomial to simultaneously fit the continuum and emission line.[1] The uncertainties on the derived emission line parameters, like the line FWHM, flux, central wavelength, and so on, were estimated using a Monte Carlo simulation (following the same methodology as Álvarez-Márquez et al. 2021, 2022). Systemic velocity shifts were removed using a heliocentric radial velocity of 278 $\pm$ 7 km

---

[1] We used the MPFIT (Markwardt 2009) Python routine to perform the fits, the code is publicly available here.

s^{-1} (Reid & Parker 2006; Margon et al. 2020). Table 1 presents the measured wavelengths and fluxes together with the identification of the mid-IR emission lines in SMP LMC 058 spectra. The residual scatter in the measured wavelengths is consistent with estimates of the $\sim$ 6 km s^{-1} MRS FLT-5 calibration accuracy (see discussion by Argyriou et al. 2023). Weak lines are more prevalent at shorter wavelengths in channels 1 and 2 where the MRS sensitivity is higher and the uncertainties in the flux are better constrained.

4 MRS RESOLVING POWER

The resolving power (R) is defined as $\lambda/\Delta\lambda$, where $\Delta\lambda$ is the minimum distance to distinguish two features in a spectrum. We define the $\Delta\lambda$ as the FWHM of an unresolved emission line. SMP LMC 058 is the only source observed in the *JWST* commissioning data sets that is considered both spatially and spectrally unresolved (with regard to the atomic emission lines) with the MRS, this makes it an excellent target for determining the inflight MRS resolving power. Here, we assume the intrinsic width of the atomic emission lines in SMP LMC 058 to be negligible, as we do not have high-resolution spectroscopy to characterize its intrinsic velocity dispersion. Nearby PN eject gas with typical velocity dispersions of about 10–51 km s^{-1} (Reid & Parker 2006). If this is the case for SMP LMC 058, then assuming a velocity of 25 km s^{-1} we might underestimate the MRS resolving power by up to 5 per cent for channel 1, and up to 1 per cent for channel 4 (see e.g. Law et al. 2021).

The pre-launch MRS resolving power has been established from MIRI ground-based test and calibration campaigns, using a set of etalons, which provided lines in all MRS bands. It was determined to be in the range of about 4000–1500 (Labiano et al. 2021). Fig. 5 shows the comparison between the ground-based MRS resolving power estimates and the inflight estimates derived from the SMP LMC 058 spectra. The inflight MRS resolving power has been determined using only emission lines with SNR higher than 6, and following the FWHM results obtained in the one- and two-component Gaussian fits (see Section 3). In the case of HI emission lines, we used the FWHM of the narrow Gaussian component. The errors in the resolving power are, on average, larger for the H I emission lines due to the uncertainty in the two-component Gaussian fit. Given the uncertainties, the inflight MRS-resolving power agrees with the ground-based estimates, and it presents a trend followed by the equation

$$R(\lambda) = 4603 - 128 \times \lambda[\mu m] + 10^{-7.4 \times \lambda[\mu m]}. \tag{1}$$

The ground-based estimates consider the width of the etalon emission lines to be negligible, which could imply an underestimation of the MRS-resolving power by a factor of 10 per cent. A similar situation is potentially happening with the inflight estimations due to the lack of the intrinsic velocity dispersion of SMP LMC 058. We conclude that the estimations of the ground-based MRS-resolving power (Labiano et al. 2021) are valid, within a 10 per cent of uncertainty, for the MRS inflight performance. As *JWST* observes more sources with spatially and spectrally unresolved spectral lines, their characterization will provide a more comprehensive understanding of the inflight variations of the resolving power within each of the 12 spectral bands. As of now, the continuous 'trend' curve in Fig. 5 presents the state of knowledge of the MRS-resolving power.

Table 1. Measured central wavelengths, line flux, line widths, and line identification for SMP LMC 058. The systemic velocity was removed prior to calculating the velocity shift of a line. If a line is present in multiple MRS bands, measurements are provided for each individual MRS segment after a flux scaling factor has been applied.

Band	Line Identification	λ_{lab} μm	$\lambda_{observed}$ μm	$\sigma\lambda_{observed}$ μm	λ_{offset} km s^{-1}	FWHM km s^{-1}	σFWHM km s^{-1}	Flux ($\times 10^{-15}$) erg s^{-1} cm^{-2}	σ ($\times 10^{-15}$) erg s^{-1} cm^{-2}
1S	H I 23−7	4.924	4.92888	0.00036	−36.700	50.006	0.354	0.05	0.01
1S	H I 22−7	4.971	4.97548	0.00013	1.092	81.360	14.817	0.10	0.01
1S	H I 21−7	5.026	5.03059	0.00009	9.737	73.767	1.100	0.09	0.02
1S	H I 20−7	5.091	5.09597	0.00005	4.404	50.000	4.146	0.09	0.02
1S	H I 10−6	5.129	5.13323	0.00001	11.008	91.157	1.145	1.67	0.02
1S	H I 19−7	5.169	5.17383	0.00006	14.639	78.964	5.807	0.14	0.01
1S	H I 18−7	5.264	5.26835	0.00006	12.574	74.052	6.568	0.15	0.02
1S	[Fe II]	5.340	5.34490	0.00009	12.537	67.901	11.809	0.06	0.01
1S	H I 17−7	5.380	5.38465	0.00005	6.445	80.560	13.568	0.19	0.02
1S	H I 16−7	5.525	5.53037	0.00003	−2.822	70.278	6.433	0.24	0.02
1S	H I 15−7	5.711	5.71656	0.00003	10.812	74.548	3.956	0.29	0.02
1M	H I 15−7	5.711	5.71681	0.00004	−2.554	83.412	5.392	0.25	0.02
1M	H I 9−6	5.908	5.91359	0.00001	5.403	92.157	1.259	2.27	0.04
1M	H I 14−7	5.957	5.96218	0.00004	9.560	88.577	3.947	0.38	0.02
1M	[K IV]	5.982	5.98787	0.00011	−15.674	79.335	14.445	0.09	0.01
1M	H I 13−7	6.292	6.29761	0.00004	6.860	79.420	4.690	0.47	0.03
1L	H I 12−7	6.772	6.77819	0.00001	3.630	83.820	1.616	0.59	0.02
1L	H I 21−8	6.826	6.83215	0.00013	3.098	99.481	19.478	0.09	0.02
1L	H$_2$(0,0) S(5)	6.910	6.91573	0.00016	8.862	91.605	10.969	0.11	0.02
1L	H I 20−8	6.947	6.95288	0.00012	14.039	73.316	13.217	0.08	0.02
1L	[Ar II]	6.985	6.99165	0.00001	4.671	87.664	1.052	1.19	0.01
1L	H I 19−8	7.093	7.09923	0.00009	2.620	62.794	6.562	0.09	0.01
1L	H I 18−8	7.272	7.27853	0.00013	−5.182	78.068	12.788	0.10	0.01
1L	[Na III]	7.318	7.32456	0.00007	−2.741	136.659	8.951	0.49	0.03
1L	H I 6−5	7.460	7.46666	0.00001	4.907	78.844	0.318	11.59	0.05
1L	H I 8−6	7.502	7.50936	0.00001	3.950	76.638	0.636	3.90	0.07
1L	H I 11−7	7.508	7.51499	0.00002	3.142	72.973	2.467	0.72	0.02
2S	H I 15−8	8.155	8.16265	0.00011	−7.101	90.115	22.497	0.23	0.04
2S	H I 14−8	8.665	8.67260	0.00007	−2.022	63.309	15.782	0.15	0.03
2M	H I 10−7	8.760	8.76835	0.00004	−5.273	95.058	4.011	0.92	0.04
2M	[Ar III]	8.991	8.99945	0.00001	9.079	95.043	0.450	20.35	0.08
2M	H I 13−8	9.392	9.40067	0.00005	2.043	81.025	5.752	0.29	0.03
2M	H$_2$(0,0) S(3)	9.665	9.67352	0.00023	11.069	126.523	25.282	0.19	0.03
2M	H I 18−9	9.847	9.85636	0.00020	−5.691	75.089	15.292	0.07	0.01
2L	[S IV]	10.511	10.51997	0.00001	8.187	93.006	0.353	29.94	0.11
2L	H I 16−9	10.804	10.81342	0.00031	5.824	84.626	17.394	0.12	0.02
2L	H I 9−7	11.309	11.31891	0.00006	7.346	79.917	3.328	1.21	0.06
3S	H I 7−6	12.372	12.38329	0.00001	2.219	96.311	0.551	5.68	0.05
3S	H I 11−8	12.387	12.39839	0.00006	6.550	95.948	3.326	0.66	0.02
3S	H I 14−9	12.587	12.59901	0.00022	−6.041	87.309	12.233	0.14	0.03
3S	[Ne II]	12.814	12.82546	0.00001	−0.298	93.821	0.237	17.58	0.04
3M	H I 13−9	14.183	14.19566	0.00029	12.515	73.945	14.232	0.20	0.04
3M	[Cl II]	14.368	14.37954	0.00018	33.363	90.252	10.042	0.35	0.04
3M	H I 16−10	14.962	14.97505	0.00018	21.949	50.004	0.148	0.06	0.02
3L	[Ne III]	15.555	15.56957	0.00002	−0.675	135.545	0.856	165.06	1.02
3L	H I 10−8	16.209	16.22345	0.00022	12.931	94.137	5.499	0.59	0.05
3L	H I 12−9	16.881	16.89658	0.00018	−5.117	88.578	7.354	0.28	0.02
4S	[S III]	18.713	18.72913	0.00002	19.760	137.009	0.492	11.30	0.05
4S	H I 8−7	19.062	19.07899	0.00005	9.471	148.337	3.018	2.39	0.05
4M	[Ar III]	21.830	21.84986	0.00069	8.268	175.623	22.240	0.82	0.09
4M	H I 13−10 + H I 11−9	22.340	22.35556	0.00054	75.494	168.816	14.574	0.65	0.14

5 DISCUSSION

5.1 Emission lines

Short-High and Long-High *Spitzer* spectroscopic data of SMP LMC 058 were published in Bernard-Salas et al. (2008). A comparison of the MRS line fluxes with those found by Bernard-Salas et al. (2008) is given in Table 2. In general, there is good agreement between our measurements of the forbidden emission line strengths of [S IV], [Ne II], [Ne III], and [S III]. Furthermore, the high-excitation lines of [Ar V] at 13.10 μm and [O IV] with ionization potentials of 60 eV and 55 eV, respectively, are not detected in either spectrum. These lines are excited by high-temperature stars with T_{eff} between 140 000 and 180 000 K. The highest ionization species in the MRS spectra are [K IV] (46 eV) and [Na III] (47 eV), these lines have not been

Table 2. Comparison of SMP LMC 058 MRS line fluxes with those of Bernard-Salas et al. ([2008](#)) taken with the high-resolution modules on the *Spitzer* IRS. All line strengths reported by Bernard-Salas et al. ([2008](#)) have a 10 per cent error except for [S IV], which has a 10 per cent–20 per cent error. Errors in the MRS flux are <1 per cent and are provided for each line in Table [1](#).

Line	Wavelength (Rest) μm	MRS flux $\times 10^{-15}$ erg s^{-1} cm^{-2}	*Spitzer* flux $\times 10^{-15}$ erg s^{-1} cm^{-2}	Ionization potential (eV)
[S IV]	10.511	29.99	29.2	35
[Ne II]	12.814	17.58	20.6	22
[Ar V]	13.099	<0.029	<2.4	60
[Ne V]	14.323	<0.005	<3.8	97
[Ne III]	15.555	165.06	200.6	41
[S III]	18.713	11.30	11.0	23
[O IV]	25.883	<0.23	<21.6	55

previously detected by *Spitzer*. Thus, we consider SMP LMC 058 to be a low-excitation source.

Given the superior sensitivity of *JWST* (Rigby et al. [2022](#)) and the MRS, we detect a line at 14.38 μm an order of magnitude below the upper-limit of [Ne V] reported by Bernard-Salas et al. ([2008](#)), which has a rest wavelength of 14.323 μm. The ionization potential of [Ne V] is 97 eV, thus it is unlikely given the absence of other high-excitation lines in the MRS spectra of SMP LMC 058, that this emission is from [Ne V], instead, we attribute this line to [Cl II], which has an ionization potential of 13 eV and a rest wavelength of 14.368 μm. This identification is consistent with the small wavelength offsets in the current MRS wavelength solution. An upper limit for the [Ne V] line at 14.323 μm is given in Table [2](#).

As seen in Table [1](#) higher ionization potential species expand at a lower velocity than the lower ionization potential species (e.g. Reid & Parker [2006](#)). This is due to ionization occurring at a greater distance from the centre of the PN where velocities are greater and can cause lower excitation species to expand to larger radii in the PN.

Hydrogen recombination lines are abundant in the spectrum of SMP LMC 058, all are new detections. H I emission lines more closely trace the ionized regions, compared to molecular hydrogen. As shown in Fig. [4](#), the line profiles of the bright H I emission lines are asymmetric, exhibiting a blue tail, whereas the forbidden emission lines present symmetric unresolved profiles. This difference in behaviour is seen even when the lines have a similar SNR, thus unlikely due to a calibration artefact. H I emission lines are composed of a spectrally unresolved main component containing the majority of the line flux (>95 per cent), and a spectrally resolved blue-shifted component possibly due to thermal broadening (Chu et al. [1984](#)) or from condensation outside the main core, which may be evident as a marginally resolved envelope like structure in the MRS cube at 7.466 μm.

Hydrogen recombination lines can be used as a diagnostic for the circumstellar envelope as the line strengths are sensitive to the density of the emitting gas. Low-density gas ($100 < N_e < 10^4$ cm^{-3} and $5000 < T_e < 10^4$ K) produces optically thin lines characterized by Case B recombination (Baker & Menzel [1938](#); Storey & Hummer [1995](#)). We compute the observed H I flux ratios, normalized to the H I 6–5 line, and compare the observed flux ratio to the expected intrinsic flux ratio from Hummer & Storey ([1987](#)) assuming Case B recombination. In Fig. [6](#), we show these values as a function of wavelength compared to the differences that would be expected due to dust extinction following the mid-IR extinction curves of Gordon et al. ([2021](#)). While there is marginal evidence for a dip

in line intensity due to absorption at ~10-micron, the observational uncertainties are too large to allow us to reliably distinguish between extinctions in the range $A_V = 2-6$.

Two molecular hydrogen lines (H$_2$) have been detected in the MRS data, the ortho-H$_2$ $v = 0$–0 S(3) and S(5) lines. The S(1) line at 17.055 μm may also be present, although this is not easily discerned above the continuum and we do not measure its flux. The S(3) and S(5) rotational line emission probably originate from irradiated, and perhaps also shocked, dense molecular clumps, torus structures (e.g. Kastner et al. [1996](#); Hora, Latter & Deutsch [1999](#); Akras, Gonçalves & Ramos-Larios [2017](#); Fang et al. [2018](#)), or from the outer regions of the PNe where the temperature is about 1000 K (Aleman & Gruenwald [2004](#); Matsuura et al. [2007b](#)).

5.2 Dust and PAH features

The dust in SMP LMC 058 is carbon-rich. Amongst the most prominent features is the strong SiC emission at 11 μm and the rising continuum due to the thermal emission of warm dust. Strong emission features from PAHs also appear in the spectrum at 5.2, 5.7, 6.2, 7.7, 8.6, 11.2, and 12.7 μm.

At sub-solar metallicities (~0.2−0.5 Z$_\odot$), SiC is commonly observed in PNe, yet it is rarely seen in Galactic PNe or indeed during the earlier AGB evolutionary phase of metal-poor carbon stars (Casassus et al. [2001](#); Zijlstra et al. [2006](#); Stanghellini et al. [2007](#); Matsuura et al. [2007a](#); Bernard-Salas et al. [2008](#); Woods et al. [2011](#), [2012](#); Sloan et al. [2014](#); Ruffle et al. [2015](#); Jones et al. [2017](#)). The strength of the SiC flux in metal-poor PNe is highly sensitive to the radiation field (Bernard-Salas et al. [2009](#)). This is likely due to a lower abundance of Si affecting the carbonaceous dust condensation sequence on the AGB. In this case, rather than SiC forming first, it instead forms in a mantle surrounding an amorphous carbon core (Lagadec et al. [2007](#); Leisenring, Kemper & Sloan [2008](#)). Then as the PNe dust becomes heated and photoprocessed, the amorphous carbon evaporates increasing the SiC surface area and consequently, its feature strength, until a critical ionization potential of >55 eV occurs at which point the SiC features disappear (Bernard-Salas et al. [2009](#); Sloan et al. [2014](#)).

Dust is expected to undergo substantial evolution during the lifetime of a PN due to sputtering and grain-grain collisions, which both 'erode' and 'shatter' the material (Lenzuni, Natta & Panagia [1989](#); Jones, Tielens & Hollenbach [1996](#)). Coagulation through grain–grain collisions altering the grain size distribution may also be expected. However, the expected time-scales for this dust evolution are unclear due to limited theoretical models of this stage. *Spitzer* IRS observations of SMP LMC 058 were obtained on 2005 June 21, 6284 d prior to our *JWST*/MRS observation of the source, thus enabling a temporal study of dust evolution in a PNe on a 17-yr time-scale. Following Bernard-Salas et al. ([2009](#)), we measure the strength of the SiC feature by integrating the flux above a continuum-subtracted spectrum from 9 to 13.2 μm and then subtracting the flux contributions from the 11.2-μm PAH feature and the [Ne II] line. Due to the resolution of the MRS compared to the *Spitzer* spectra of SMP LMC 058, we detect several additional lines, which contribute to the integrated flux in the SiC region; these lines include [S IV] and H I. Thus to obtain a reliable measurement of the SiC feature strength we also subtract the flux contribution from all emission lines in the 9–13.2-μm region listed in Table [1](#). A PAH feature at ~12.6 μm likely contributes a small amount of flux to the measured SiC feature, however, isolating and subtracting this emission contribution from the wing of the SiC feature is challenging even with the
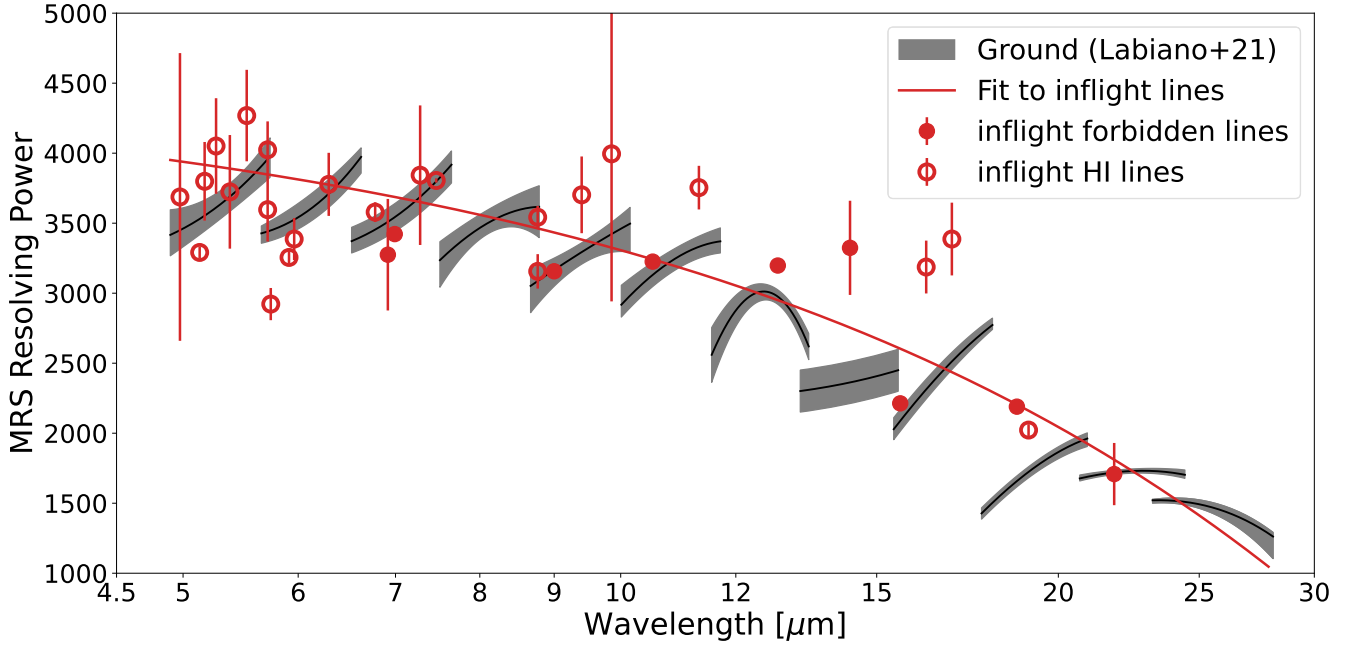
Figure 5. Comparison between the ground-based and inflight MRS-resolving power. Grey filled area and black line: ground-based MRS-resolving power estimates (Labiano et al. 2021). Filled red circles: inflight MRS-resolving power calculation using forbidden emission lines identified in this paper. Open red circles: inflight MRS-resolving power calculation using H I emission lines.
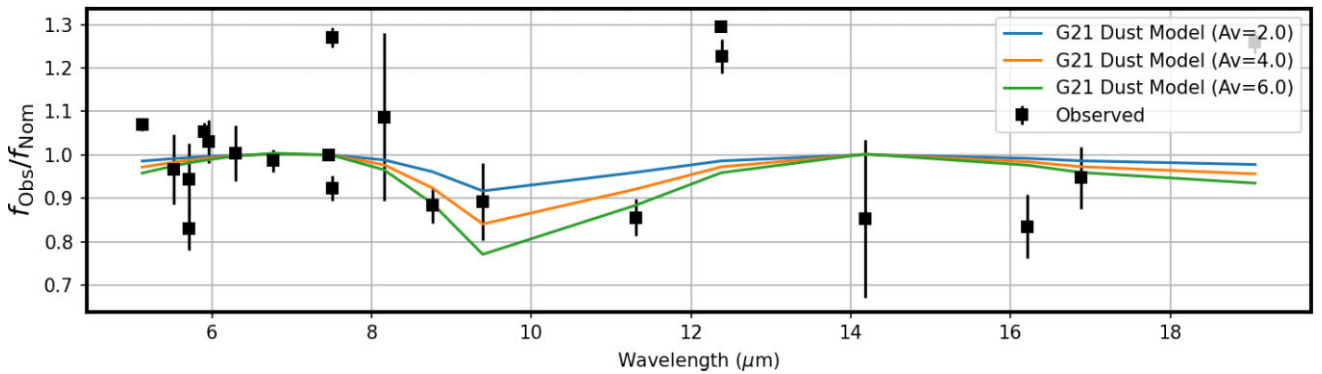

Figure 6. Comparison of the nominal H I line ratios f_{Norm} from Hummer & Storey (1987) and our observed ratios f_{Obs} for SMP LMC 058. Models of dust extinction as a function of wavelength for a range of A_V taken from Gordon et al. (2021) are also shown.

Table 3. PAH and SiC fluxes and centroids.

	Centroid μm	Integrated flux W m^{-2}	Integrated flux error W m^{-2}
PAH	5.262	1.64×10^{-18}	7.0×10^{-20}
PAH	5.698	5.62×10^{-18}	1.1×10^{-19}
PAH	6.274	9.259×10^{-17}	2.9×10^{-19}
PAH	7.834	3.427×10^{-16}	1.2×10^{-18}
PAH	8.665	6.231×10^{-17}	8.5×10^{-19}
PAH	11.298	1.047×10^{-16}	2.0×10^{-18}
SiC	11.097	3.067×10^{-15}	4.5×10^{-18}

MRS spectral resolution. Additionally, an artefact at $\sim$12.2 μm due to a spectral leak (e.g. Gasman et al. 2022) may also affect the integrated flux. Table 3 gives the measured SiC centroid and corrected feature strength. The latter agrees exceptionally well with the value of $29.72 \pm 0.31 \times 10^{-16}$ W m^{-2} measured by Bernard-Salas et al. (2009) in the *Spitzer* data of SMP LMC 058. This

suggests there is little to no evolution in the SiC dust on the 17-yr time-scales between the observations. Furthermore, the agreement between the measurements verifies the overall flux calibration of the MRS instrument (Gasman et al. 2022).

In astronomical sources, the structure, wavelengths and relative strength of the PAHs can differ strongly between objects, with PNe showing the most pronounced variations in PAH profiles due to photoprocessing altering the ratio of aliphatics to aromatics (Peeters et al. 2002; Pino et al. 2008; Matsuura et al. 2014; Sloan et al. 2014; Jensen et al. 2022). Fig. 7 shows the PAHs in SMP LMC 058. The PAHs in SMP LMC 058 are considered to have a class B profile by Bernard-Salas et al. (2009) and Sloan et al. (2014). In this schema devised by Peeters et al. (2002) and van Diedenhoven et al. (2004), the 6.2 PAH feature for class B objects has a peak between 6.24 and 6.28 μm; the dominant 7.7 PAH feature peaks between 7.8 and 8.0 μm; and the 8.6 PAH band is red-shifted. These values agree well with our measured centroids listed in Table 3. Furthermore, the PAHs observed in SMP LMC 058
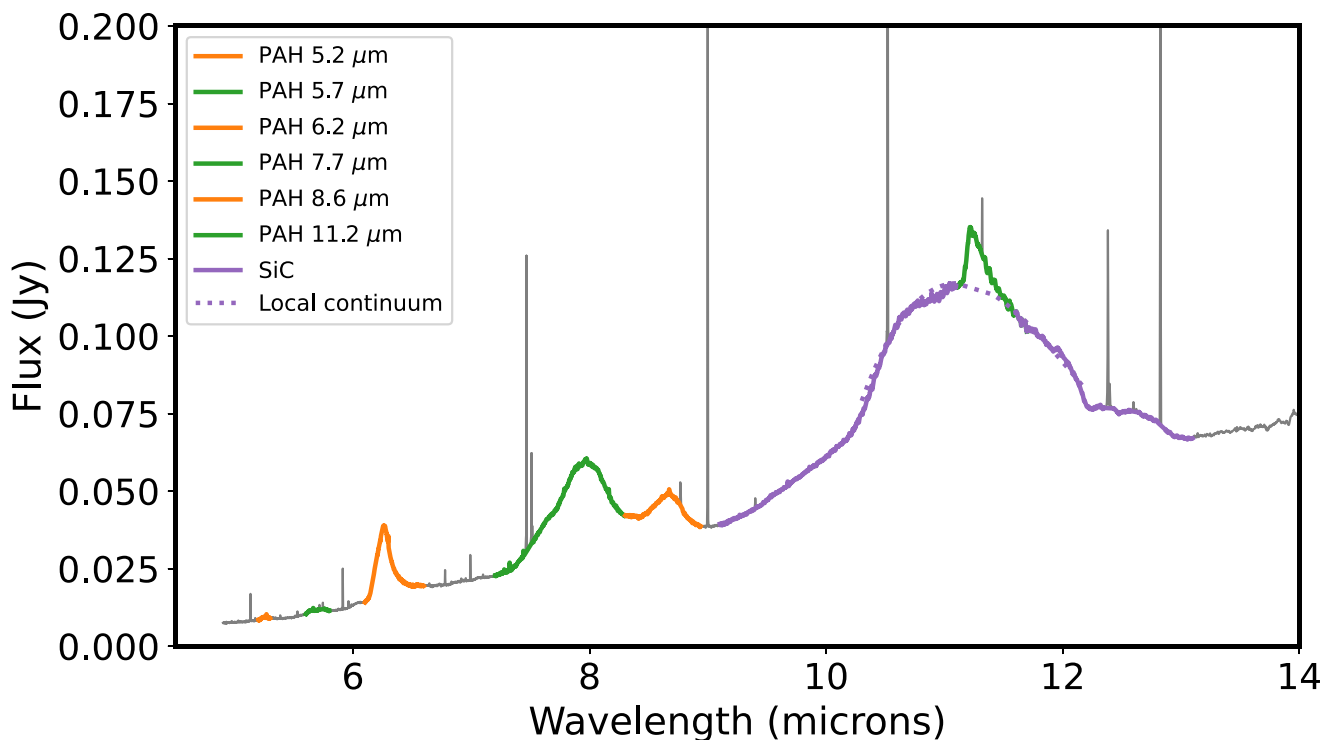
Figure 7. The SiC and PAH features are highlighted in the spectra of SMP LMC 058. A local continuum fit to the 11.3 μm feature, which is superimposed on the broad SiC emission feature is also shown. The colours highlight the spectral region for each feature, to which a local continuum was fit and the flux measured over.

closely resemble those observed in the *ISO* SWS spectrum of the Galactic post-AGB star, HD 44 179 (the Red Rectangle), which also shows strong aromatic features on top of a continuum (Waters et al. 1998).

The relative strength of the PAH features depends on a number of factors including the degree of ionization of the radiation field (e.g. Allamandola, Hudgins & Sandford 1999). The strength of the PAH features in SMP LMC 058 was measured by integrating the flux of the feature above an adopted local continuum, fit to each side of the feature and measured using SPECUTILS LINE_FLUX. Particular care was taken in fitting a continuum, too, and then measuring the 11.25-μm band (produced by the out-of-plane solo C–H bending mode) as this is superimposed on top of the broad SiC feature. Table 3 presents the central wavelength of the features and the integrated flux. The ratio of the PAH strengths correlates with the source type, and hence its physical conditions (Hony et al. 2001); ionized PAHs have strong features at 6.2, 7.7, and 8.6 μm whilst the 11.2-μm PAH feature is stronger for neutral PAHs. From the PAH line strengths given in Table 3 it is evident that the 7.7-μm feature dominates the total PAH emission.

Carbon-rich PNe can show a rich variety of solid-state material in their spectra in addition to PAHs. The C_{60} fullerene molecule typically exhibits features at ~7.0, 8.5, 17.4, and 18.9 μm, and all four were first identified in the spectrum of the Galactic PN TC-1 (Cami et al. 2010). Fullerenes have since been detected in several other PNe (e.g. García-Hernández et al. 2010, 2011; Sloan et al. 2014). The still-unidentified 21 μm emission feature, first detected by Kwok, Volk & Hrivnak 1989, can also appear in carbon-rich PNe, often associated with unusual PAH emission and aliphatic hydrocarbons (Cerrigone et al. 2011; Matsuura et al. 2014; Sloan et al. 2014; Volk, Sloan & Kraemer 2020). The spectra of SMP LMC

058 from the IRS on Spitzer did not show any of these unusual hydrocarbon-related features, but the improved spectral resolution of the MRS allows for a much more careful examination. None the less, these additional features remain too weak to be detected. SMP LMC 058 presents a classic Class B PAH spectrum, as expected for objects, which have evolved to the young PN stage (Sloan et al. 2014). Younger objects, which could still be described as post-AGB objects would show the 21-μm feature and/or aliphatics. Sloan et al. (2014) identified SMP LMC 058 as a member of the Big-11 group because of the combination of a strong SiC emission feature and the 11.2-μm PAH feature and the absence of fullerenes. They also noted that the Big-11 group is related to the PNe that show fullerenes, and that the presence or absence of fullerenes may be due to something as simple as which have a clear line of sight to the interior of the dust shells where the fullerenes are expected to be present.

6 SUMMARY AND CONCLUSIONS

We have presented MIRI/MRS spectra of the carbon-rich PN SMP LMC 058 located in the Large Magellanic Cloud. SMP LMC 058 is a point source in the MRS data and its spectrum contains the only spatially and spectrally unresolved emission lines observed during the commissioning of the *JWST* MRS. In the MRS spectrum, we detected 51 emission lines, of which 47 were previously undetected in this source. The strongest emission lines were used to determine the spectral resolutions of the MIRI MRS instrument. The resolving power is $R > 3660$ in channel 1, $R > 3430$ in channel 2, $R > 3200$ in channel 3, and $R > 1920$ in channel 4. This on-sky performance is comparable to the resolution determined from the ground calibration of the MRS, which provides resolving powers from 4000 at channel 1 to 1500 at channel 4. Furthermore, a comparison of the line strengths

and spectral continuum to previous observations of SMP LMC 058 with the IRS on the *Spitzer* was used to verify the absolute flux calibration of the MRS instrument. The MRS spectra confirm that the carbon-rich dust emission is from grains and not isolated molecules and that there is little to no time evolution of the SiC dust and emission line strengths in the 17 yr between the observations. The PAH emission is dominated by the 7.7-μm feature. The strong PAHs and SiC in the spectra are consistent with the lack of high-excitation lines detected in the spectra, which if present, would indicate a hard radiation field that would likely destroy these grains. These commissioning data reveal the great potential and resolving power of the MIRI MRS to study line, molecular, and solid-state features in individual sources in nearby galaxies.

DATA AVAILABILITY

JWST data were obtained from the Mikulski Archive for Space Telescopes at the Space Telescope Science Institute (https://archive.stsci.edu/).

REFERENCES

Akras S., Gonçalves D. R., Ramos-Larios G., 2017, MNRAS, 465, 1289
Aleman I., Gruenwald R., 2004, ApJ, 607, 865
Allamandola L. J., Hudgins D. M., Sandford S. A., 1999, ApJ, 511, L115
Álvarez-Márquez J., Marques-Chaves R., Colina L., Pérez-Fournon I., 2021, A&A, 647, A133
Álvarez-Márquez J. et al., 2022, A&A, 672, A108
Argyriou I. et al., 2023, preprint (arXiv:2303.13469)
Baker J. G., Menzel D. H., 1938, ApJ, 88, 52
Bernard-Salas J., Pottasch S. R., Gutenkunst S., Morris P. W., Houck J. R., 2008, ApJ, 672, 274
Bernard-Salas J., Peeters E., Sloan G. C., Gutenkunst S., Matsuura M., Tielens A. G. G. M., Zijlstra A. A., Houck J. R., 2009, ApJ, 699, 1541
Brown M. J. I., Jarrett T. H., Cluver M. E., 2014, PASA, 31, e049
Bushouse H. et al., 2022, spacetelescope/jwst: JWST 1.6.2. Zenodo. doi:10.5281/zenodo.6984366
Cami J., Bernard-Salas J., Peeters E., Malek S. E., 2010, Science, 329, 1180
Casassus S., Roche P. F., Aitken D. K., Smith C. H., 2001, MNRAS, 327, 744
Cerrigone L., Hora J. L., Umana G., Trigilio C., Hart A., Fazio G., 2011, ApJ, 738, 121
Choudhury S., Subramaniam A., Cole A. A., 2016, MNRAS, 455, 1855
Chu Y. H., Kwitter K. B., Kaler J. B., Jacoby G. H., 1984, PASP, 96, 598
Fang X., Zhang Y., Kwok S., Hsia C.-H., Chau W., Ramos-Larios G., Guerrero M. A., 2018, ApJ, 859, 92
Feuchtgruber H. et al., 1997, ApJ, 487, 962
García-Hernández D. A., Górny S. K., 2014, A&A, 567, A12
García-Hernández D. A., Manchado A., García-Lario P., Stanghellini L., Villaver E., Shaw R. A., Szczerba R., Perea-Calderón J. V., 2010, ApJ, 724, L39
García-Hernández D. A. et al., 2011, ApJ, 737, L30
Gasman D. et al., 2022, A&A, 673, 17
Gonçalves D. R., Magrini L., Teodorescu A. M., Carneiro C. M., 2014, MNRAS, 444, 1705

Gordon K. D., Engelbracht C. W., Rieke G. H., Misselt K. A., Smith J. D. T., Kennicutt Robert C. J., 2008, ApJ, 682, 336

Gordon K. D. et al., 2021, ApJ, 916, 33

Guzman-Ramirez L., Zijlstra A. A., Níchuimín R., Gesicki K., Lagadec E., Millar T. J., Woods P. M., 2011, MNRAS, 414, 1667

Hony S., Van Kerckhoven C., Peeters E., Tielens A. G. G. M., Hudgins D. M., Allamandola L. J., 2001, A&A, 370, 1030

Hora J. L., Latter W. B., Deutsch L. K., 1999, ApJS, 124, 195

Houck J. R. et al., 2004, in Mather J. C.ed., SPIE Conf. Ser., Vol. 5487, Optical, Infrared, and Millimeter Space Telescopes. SPIE, Cergy-Pontoise, p. 62,

Hummer D. G., Storey P. J., 1987, MNRAS, 224, 801

Jensen P. A., Shannon M. J., Peeters E., Sloan G. C., Stock D. J., 2022, A&A, 665, A153

Jones A. P., Tielens A. G. G. M., Hollenbach D. J., 1996, ApJ, 469, 740

Jones O. C. et al., 2017, MNRAS, 470, 3250

Karakas A., Lattanzio J. C., 2007, PASA, 24, 103

Karakas A. I., Lattanzio J. C., 2014, PASA, 31, e030

Karakas A. I., Lattanzio J. C., Pols O. R., 2002, PASA, 19, 515

Kastner J. H., Weintraub D. A., Gatley I., Merrill K. M., Probst R. G., 1996, ApJ, 462, 777

Kemper F. et al., 2010, PASP, 122, 683

Kendrew S. et al., 2015, PASP, 127, 623

Kester D. J. M., Beintema D. A., Lutz D., 2003, in Metcalfe L., Salama A., Peschke S. B., Kessler M. F.eds, The Calibration Legacy of the ISO Mission. Vol. 481, ESA Special Publication, European Space Agency, Paris, p. 375

Kwitter K. B., Henry R. B. C., 2022, PASP, 134, 022001

Kwok S., 2000, The Origin and Evolution of Planetary Nebulae, Cambridge Univ. Press, Cambridge

Kwok S., Volk K. M., Hrivnak B. J., 1989, ApJ, 345, L51

Labiano A. et al., 2016, in Observatory Operations: Strategies, Processes, and Systems VI. SPIE, Cergy-Pontoise, p. 99102W

Labiano A. et al., 2021, A&A, 656, A57

Lagadec E. et al., 2007, MNRAS, 376, 1270

Law D. R. et al., 2021, AJ, 161, 52

Leisenring J. M., Kemper F., Sloan G. C., 2008, ApJ, 681, 1557

Lenzuni P., Natta A., Panagia N., 1989, ApJ, 345, 306

Madau P., Ferguson H. C., Dickinson M. E., Giavalisco M., Steidel C. C., Fruchter A., 1996, MNRAS, 283, 1388

Margon B., Massey P., Neugent K. F., Morrell N., 2020, ApJ, 898, 85

Markwardt C. B., 2009, in Bohlender D. A., Durand D., Dowler P.eds, ASP Conf. Ser.. Vol. 411, Astronomical Data Analysis Software and Systems XVIII. Astron. Soc. Pac., San Francisco, p. 251

Matsuura M. et al., 2007a, MNRAS, 382, 1889

Matsuura M. et al., 2007b, MNRAS, 382, 1447

Matsuura M. et al., 2014, MNRAS, 439, 1472

Pagomenos G. J. S., Bernard-Salas J., Pottasch S. R., 2018, A&A, 615, A29

Peeters E., Hony S., Van Kerckhoven C., Tielens A. G. G. M., Allamandola L. J., Hudgins D. M., Bauschlicher C. W., 2002, A&A, 390, 1089

Perley R. A., Butler B. J., 2013, ApJS, 204, 19

Pietrzyński G. et al., 2013, Nature, 495, 76

Pino T. et al., 2008, A&A, 490, 665

Reid W. A., 2014, MNRAS, 438, 2642

Reid W. A., Parker Q. A., 2006, MNRAS, 373, 521

Reid W. A., Parker Q. A., 2010, MNRAS, 405, 1349

Rigby J. et al., 2022, PASP, 135, 31

Ruffle P. M. E. et al., 2015, MNRAS, 451, 3504

Sanduleak N., MacConnell D. J., Philip A. G. D., 1978, PASP, 90, 621

Sloan G. C. et al., 2014, ApJ, 791, 28

Stanghellini L., García-Lario P., García-Hernández D. A., Perea-Calderón J. V., Davies J. E., Manchado A., Villaver E., Shaw R. A., 2007, ApJ, 671, 1669

Storey P. J., Hummer D. G., 1995, MNRAS, 272, 41

Swinyard B. M. et al., 1996, A&A, 315, L43

Volk K., Sloan G. C., Kraemer K. E., 2020, Ap&SS, 365, 88

Waters L. B. F. M. et al., 1996, A&A, 315, L361

Waters L. B. F. M. et al., 1998, Nature, 391, 868

Wells M. et al., 2015, PASP, 127, 646

Westerlund B. E., 1997, Cambridge Astrophysics Series, Cambridge Univ. Press, Cambridge, p. 29

Woods P. M. et al., 2011, MNRAS, 411, 1597

Woods P. M., Walsh C., Cordiner M. A., Kemper F., 2012, MNRAS, 426, 2689

Wright E. L. et al., 2010, AJ, 140, 1868

Zijlstra A. A. et al., 2006, MNRAS, 370, 1961

Ziurys L. M., 2006, Proc. Natl. Acad. Sci., 103, 12274

de Graauw T. et al., 1996, A&A, 315, L49

van Diedenhoven B., Peeters E., Van Kerckhoven C., Hony S., Hudgins D. M., Allamandola L. J., Tielens A. G. G. M., 2004, ApJ, 611, 928

This paper has been typeset from a TEX/LATEX file prepared by the author.